Measurement of the x-ray mass attenuation coefficient and determination of the imaginary component of the atomic form factor of molybdenum over the 13.5–41.5-keV energy range

Martin D. de Jonge, Chanh Q. Tran, Christopher T. Chantler, Zwi Barnea, and Bipin B. Dhal
School of Physics, University of Melbourne, Melbourne, Victoria 3010, Australia

David J. Cookson*
Chem-Mat-CARS, Argonne National Laboratory, 9700 South Cass Avenue, Argonne, Illinois 60439, USA

Wah-Keat Lee and Ali Mashayekhi
XOR 1-ID, Argonne National Laboratory, 9700 South Cass Avenue, Argonne, Illinois 60439, USA
(Received 19 July 2004; published 4 March 2005)

We use the x-ray extended-range technique (XERT) [Chantler *et al.*, Phys. Rev. A **64**, 062506 (2001)] to measure the mass attenuation coefficients of molybdenum in the x-ray energy range of 13.5–41.5 keV to 0.02–0.15 % accuracy. Measurements made over an extended range of the measurement parameter space are critically examined to identify, quantify, and correct where necessary a number of experimental systematic errors. These results represent the most extensive experimental data set for molybdenum and include absolute mass attenuation coefficients in the regions of the x-ray absorption fine structure (XAFS) and x-ray-absorption near-edge structure (XANES). The imaginary component of the atomic form-factor f_2 is derived from the photoelectric absorption after subtracting calculated Rayleigh and Compton scattering cross sections from the total attenuation. Comparison of the result with tabulations of calculated photoelectric absorption coefficients indicates that differences of 1–15 % persist between the calculated and observed values.

I. INTRODUCTION

The attenuation of x rays by materials provides a wide variety of information about the fundamental properties of matter in the atomic, molecular, and solid states. In particular, relative and absolute measurements of the mass attenuation coefficient are used to test theoretical predictions of photoelectric absorption using bound-state electron wave functions [1,2], to investigate the dynamics of atomic processes, including shake-up, shake-off, and Auger transitions [3–6], and to provide information on the density of electronic states [7], molecular bonding, and other solid-state properties [8]. The diversity of these studies is evidence of the wide variety of processes that influence the attenuation of x rays.

In order to develop a deeper understanding of the interactions between x rays and matter it is necessary to make accurate measurements, so that each attendant process may be studied and compared with theoretical models. While relative measurements are adequate for some applications, absolute attenuation measurements provide additional, crucial, and demanding tests of theoretical predictions. For example, while finite-difference calculations [9] have recently had significant success in predicting extended x-ray absorption fine structure (EXAFS) on a relative scale, they are in relatively poor agreement with the results of absolute measurements [10]. Measurement inaccuracy and discrepancies between theoretical calculations seriously impede the understanding of x-ray interactions with matter.

X-ray atomic form factors are calculated by using atomic theory, quantum mechanics, and quantum electrodynamics to describe the scattering of x rays using calculated atomic wave functions. Major differences in the calculated values of form factors result from the various theoretical frameworks that are employed for calculating these atomic wave functions, each of which treats exchange, correlation, and overlap effects in a different manner. Further differences stem from the diverse application of approximate methods employed to describe multielectron atomic wave functions.

We present in Fig. 1 a comparison between the results of two commonly used tabulations of mass attenuation coefficients for molybdenum. These results have been derived directly from form-factor calculations with small Rayleigh and Compton scattering cross sections added. The ordinate of this plot is the percentage difference from the FFAST tabulation [11–13]. This figure shows the large differences that can occur when alternate methodologies are applied, with the differences rising to around 17% in the region above the absorption edge at around 20 keV. The differences are stable at around 3–4 % in the energy region below the absorption edge and there is reasonable agreement at the higher energies shown in this figure. The presence of regions of moderate agreement and large differences suggests that the approach and the implementation of the calculation may have significant and varying consequences for the predicted values in different energy regions.

These models and their implementations can be tested by comparing tabulated and measured values. In Fig. 1 we have included the results of a number of measurements of the mass attenuation coefficient of molybdenum [14,15]. We im-

---

*Also at ANSTO, Private Mail Bag 1, Menai, New South Wales 2234, Australia.
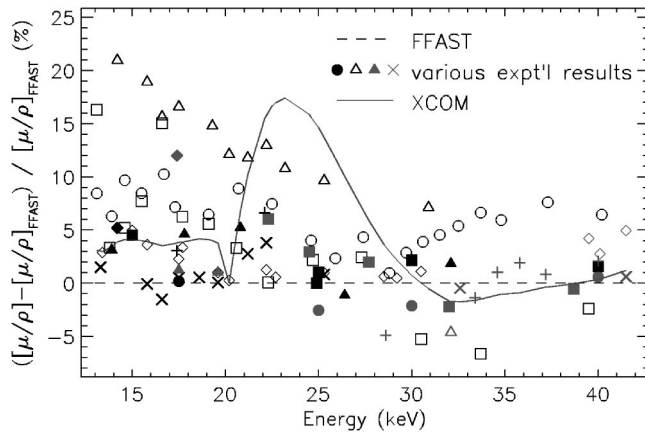
FIG. 1. Discrepancies between theoretical predictions and experimental measurements of the mass attenuation coefficient of molybdenum presented as a percentage difference from the FFAST tabulation [11–13]. The XCOM tabulation is from [16,17]. The various previously measured values have been sourced from the compilation of Hubbell *et al.* [14,15]. Multiple values arising from individual experiments are marked with the same symbol, establishing the trend of each set of measurements. The 10–20 % variation between the measured values whose typical claimed uncertainties are around 2% indicates the presence of unquantified systematic errors affecting these measurements.

mediately see from this plot that the measurements do not commend either tabulation. These reported measurements typically claim accuracies of 0.5–2 %, sufficient to decide between the theoretical values. However, despite these claimed accuracies, the different sets of measurements differ by up to 20%. In order to discriminate between the different tabulated values, measurements are required to be both accurate and precise to better than about 1% below the absorption edge, about 4% immediately above the absorption edge, and possibly 0.2% far above the absorption edge.

The discrepancies between the theories, between different experiments, and between theory and experiment have prompted the International Union of Crystallography, representing one of the world's largest group of users of form-factor data, to undertake a systematic investigation of form-factor-based calculations of mass attenuation coefficients and their measurement [18,19]. A primary conclusion of their survey of measurement techniques was that a variety of poorly understood and unquantified sources of systematic error may be adversely affecting the measurements.

The x-ray extended-range technique (XERT) [1,2] employs measurements made over an extended range of the measurement parameter space to probe systematic errors affecting the measurement. The specific extended ranges of the measurement parameter space investigated were the attenuation $[\mu/\rho][\rho t]$ of the absorbers, the x-ray energy, the angular acceptance of the detectors, the angle of the absorbing sample relative to the incident x-ray beam, and the variations in integrated column density of the absorbing foil. These parameter-space explorations sought the optimal measurement configuration but were deliberately extended outside the optimal regimes to determine the effect of systematic errors on the measurement.

In this article we report measurements of the mass attenuation coefficients of molybdenum. The results of an extensive investigation of systematic errors affecting the measurement are presented. The mass attenuation coefficients are determined to an accuracy of 0.028% away from the *K* absorption edge and 0.1% in the vicinity of the *K* absorption edge. The precision of the measurements is 0.02–0.15 % at over 500 energies between 13.5 and 41.5 keV.

This article is divided into eight sections. In Sec. II we describe the attenuating samples and the experimental setup. Section III describes the detailed interpretation of the measurements leading to the determined mass attenuation coefficients. In Sec. IV we report the method by which we determine the energy of the x rays. We provide a tabulation of the results in Sec. V, and quantify contributions to the accuracy and the precision of the results. In Sec. VI we compare our results with a variety of tabulations of the photoelectric absorption coefficients and find that the currently available tabulations differ significantly from our measured values. Section VII is a summary of our conclusions. We have relegated to the Appendix further details of the interpretation of the measurements leading to the mass attenuation coefficients.

II. EXPERIMENTAL DETAILS

A. Samples

The molybdenum foil samples were of various thicknesses between 25 and 250 μm and were all approximately 25×25 mm^2 in area as supplied by ESPI [20]. The quoted purity of all foils was 99.98%. A typical assay provided by the manufacturer listed the impurities as iron (52 ppm), potassium (40 ppm), chromium (32 ppm), nickel (25 ppm), and copper (16 ppm) [21]. The effect of these impurities on the measured mass attenuation coefficient was estimated by use of the tabulated values of their mass attenuation and found to be less than 0.01% for all measurements in the range of energies between 13.5 and 41.5 keV.

Each foil was weighed to determine its mass m using a microgram-accuracy Mettler microbalance which was buoyancy compensated for a mass of density $\rho=8.4$ g/cm^3. The residual effect of the buoyancy of the molybdenum samples (nominal density $\rho=10.2$ g/cm^3) is to alter the apparent mass by around 0.0025%, and this effect was not corrected as it is far below the measurement uncertainty. Each foil had its projected facial area A measured with a Mitutogo PJ300 traveling-stage shadow-projection optical comparator. The mass and area of each foil was used to determine its average integrated column density $\overline{[\rho t]}$ from $\overline{[\rho t]}=m/A$.

We have measured the surface roughness of a number of the foils used in this measurement using an atomic force microscope (AFM). The AFM measurements determine rms roughnesses σ_t of 200–500 nm over scan areas typically of the order of 80×80 μm^2. The effect of these measured roughnesses on the measured attenuation was evaluated from [22,23]

$$\left[\frac{\mu}{\rho}\right] \rightarrow \left[\frac{\mu}{\rho}\right]' = \left[\frac{\mu}{\rho}\right] + \frac{1}{[\rho t]}\ln\left(1 + \frac{[\mu/\rho]^2\rho^2\sigma_t^2}{2!}\right), \quad (1)$$

resulting in a correction of less than 0.004% for the foils used in this experiment. The effect of thickness variations
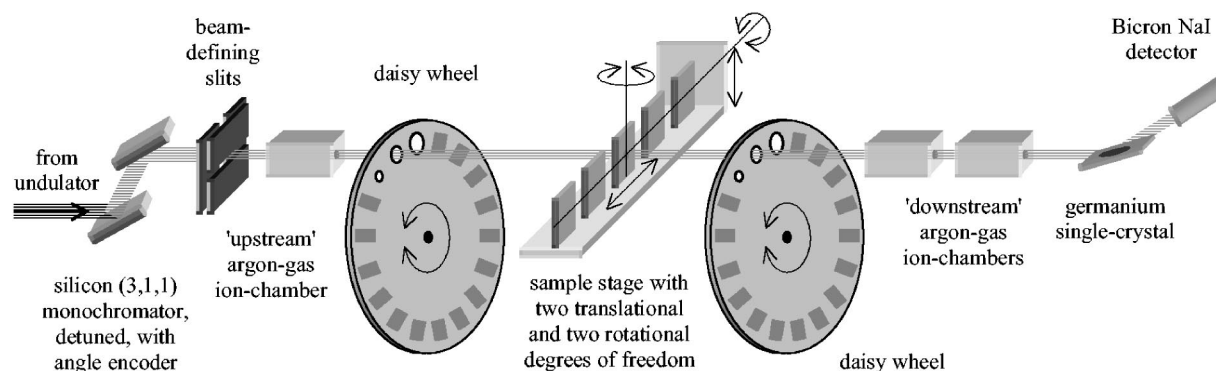
FIG. 2. Schematic of the experimental layout.

over longer length scales will be investigated in a later section.

B. Experimental components

The x-ray beam was produced by an undulator insertion device at the 1-ID XOR beamline of the Advanced Photon Source facility at the Argonne National Laboratory [24]. The (3,1,1) planes of a silicon double-reflection monochromator were used to select a narrow range of energies from the undulator spectrum. The x-ray energy range covered by this investigation, from 13.5 to 41.5 keV, includes the K-shell absorption edge of molybdenum at around 20 keV, and extends over a wide range of energies above and below the edge. The energy range was limited primarily by the operational characteristics of the synchrotron beamline facility. The energy spacing of the measurements was varied in accordance with the structure in the mass attenuation coefficient of molybdenum: it was kept down to 0.5 eV within 100 eV of the absorption edge, and was increased to 500 eV at energies far from the absorption edge.

The fifth-order component of the undulator spectrum was selected to provide x rays with energies between 41.5 and 25 keV and the third-order component for x-ray energies below 25 keV. To reduce the passage of harmonic components into the beam the second crystal in the monochromator was "detuned" slightly from its position parallel to the first crystal such that the beam intensity decreased to between 35% and 55% of its peak, undetuned value [25,26].

After monochromation the x-ray beam traveled approximately 30 m down an evacuated pipe into the experimental hutch (see Fig. 2). On entry to the hutch the x rays passed first through a beryllium window and then through a pair of orthogonal adjustable slits which defined the beam cross section to be approximately 1×1 mm^2.

The x-ray beam then passed through the first of three 95-mm-long, argon gas ion chambers. The ion chambers were of identical construction, and argon gas flowed through the detectors in series at a rate of around 1 l/min. Two downstream ion chambers were employed to improve the counting statistics, to investigate the ion chamber and electronic nonlinearities, and to provide a cross-check of the measured attenuated beam intensity.

The molybdenum samples were clamped between two Perspex holders which could slot neatly into a stainless steel base to provided wobble-free location of the sample. Five samples at a time were mounted on the stage, shown in Fig. 2, which was located midway between the upstream and the first of the downstream ion chambers. The sample thicknesses were chosen such that at each energy they typically spanned a range of attenuation $(0.3-2) \lesssim [\mu/\rho][\rho t] \lesssim (3.5-9)$. The stage could be rotated about two axes and translated in two directions orthogonal to the beam. The samples could thus be placed and replaced in the path of the beam to high precision by the use of a computer-controlled motorized driving system. The estimated reproducibility of the translation was of order 10 μm and the rotational reproducibility was of order 0.1°.

Counter normalization was determined by recording the count rates in the detectors with the samples translated out of the path of the beam. The attenuated and unattenuated intensities were measured in rapid succession at each energy by an automated movement routine.

Daisy wheels [27] were located between the sample stage and the ion chambers. These had on their perimeters three apertures subtending solid angles of 8.7, 33, and 150 μsr at the sample which were used to admit different amounts of secondary photons into the ion chambers. In addition to these apertures, 30 attenuating foils were mounted on the perimeter of the daisy wheels and these too could be placed in the path of the beam by suitable rotation of the daisy wheel. The thicknesses of these foils were chosen to span approximately three orders of magnitude in the x-ray attenuation $[\mu/\rho][\rho t]$.

III. DETERMINING THE MASS ATTENUATION COEFFICIENT

A. Intensity measurements

Counts were recorded simultaneously in the upstream u and downstream d ion chambers with a sample s interposed into the x-ray beam (recording intensities $I_{d,s}, I_{u,s}$), without a sample in the x-ray beam ($I_{d,b}, I_{u,b}$, b for blank), and with the x-ray beam shutter closed ($I_{d,d}, I_{u,d}$, d for dark). Each measurement of 0.1 s counting time was repeated ten times to yield a measure of the reproducibility of the measurement and to enable proper treatment of correlations in the counting chain [28,29].

"Dark current" measurements of the apparent count rate recorded in the absence of the x-ray beam were made regularly throughout the experiment to account for amplifier offsets. The trend of the dark current count rates was linearly interpolated within regions where the ion-chamber electronics settings were unchanged to account for any variation of this offset due, for instance, to electronic drifts. The error attributed to the dark-current count rates was one standard deviation of the results about the trend of the measured values. Dark-current counts were typically of the order of 17 ± 1 over a 0.1 s counting interval.

The upstream ion chamber was used to monitor the beam intensity and to normalize the downstream readings, thus enabling the separation of the synchrotron beam intensity fluctuations from other noise components. The normalized count rates for the blank and sample measurements were obtained from the ratio of the counts recorded simultaneously in the upstream and downstream ion chambers after subtraction of their dark currents. The counts recorded by each of the downstream ion chambers were processed separately at this and every successive stage of the calculation. The normalized intensities were determined from the mean of the ratios of ten successive measurements,

$$I_x = \overline{\left(\frac{I_{d,x} - I_{d,d}}{I_{u,x} - I_{u,d}} \right)}, \tag{2}$$

and their uncertainties were determined from

$$\sigma_{I_x} = \left\{ \mathrm{var}\left(\frac{I_{d,x} - I_{d,d}}{I_{u,x} - I_{u,d}} \right) + \left[\left(\frac{I_{d,x} - I_{d,d}}{I_{u,x} - I_{u,d}} \right) \frac{\sigma_{I_{u,d}}}{I_{u,x} - I_{u,d}} \right]^2 \right.$$
$$\left. + \left[\left(\frac{I_{d,x} - I_{d,d}}{I_{u,x} - I_{u,d}} \right) \frac{\sigma_{I_{u,d}}}{I_{u,x} - I_{u,d}} \right]^2 \right\}^{1/2}, \tag{3}$$

where the subscript x denotes the use of blank b or sample s measurements to determine the unattenuated and attenuated normalized intensities I_b and I_s and their uncertainties σ_{I_b} and σ_{I_s}, respectively. $\sigma_{I_{d,d}}$ and $\sigma_{I_{u,d}}$ are the uncertainties in the dark currents determined in the downstream and upstream detectors, respectively. As discussed elsewhere [28,29], the variance of the measurements is appropriate for the high correlation coefficient R of 0.99 between the measurements recorded with the upstream and downstream ion chambers. The additional terms in Eq. (3) are the contributions to the uncertainty in the normalized intensities arising from the corresponding uncertainties in the measured dark currents.

The attenuation $[\mu/\rho][\rho t]$ is evaluated for measurements with each sample at each energy using

$$\left[\frac{\mu}{\rho} \right][\rho t] = -\ln\left(\frac{I_s}{I_b} \right) = \ln\left[\overline{\left(\frac{I_{d,b} - I_{d,d}}{I_{u,b} - I_{u,d}} \right)} \right] - \ln\left[\overline{\left(\frac{I_{d,s} - I_{d,d}}{I_{u,s} - I_{u,d}} \right)} \right], \tag{4}$$

with the uncertainty in the attenuation determined by

$$\sigma_{[\mu/\rho][\rho t]} = \left[\left(\frac{\sigma_{I_s}}{I_s} \right)^2 + \left(\frac{\sigma_{I_b}}{I_b} \right)^2 \right]^{1/2}. \tag{5}$$
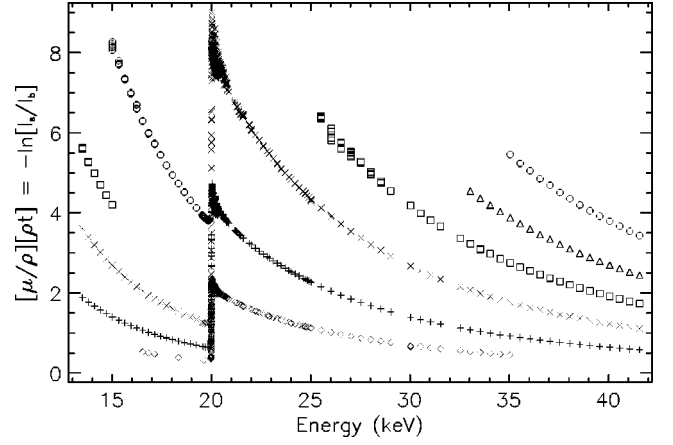
FIG. 3. Measured attenuations $-\ln(I_s/I_b) = [\mu/\rho][\rho t]$. The markers represent results obtained using foils of the following nominal thicknesses: $\diamond$, 25 μm; +, 50 μm; $\times$, 100 μm; $\square$, 150 μm; $\triangle$, 200 μm; $\bigcirc$, 250 μm. A subset of the foils was measured at each energy. The absorbers span a wide range of attenuations at each measured energy, allowing attenuation-dependent systematic errors to be detected.

We present in Fig. 3 the attenuations calculated by use of Eqs. (2)–(5). The results of the calculations using the counts recorded in the two downstream ion chambers and those with apertures of various diameters placed between the absorber and the ion chambers are plotted on this figure but cannot be resolved except where the statistical precision of the measurement is poor, particularly when the foil attenuation rises above about 5–6.

In Fig. 4 we show the percentage uncertainties for the attenuations presented in Fig. 3. This figure shows that, as expected, a higher level of uncertainty is associated with measurements where the foil attenuation differs markedly from the "optimal" Nordfors range of $2 < [\mu/\rho][\rho t] < 4$ [30]. The uncertainties presented here are in broad agreement with the statistical limit of the precision given by the Nordfors criterion. The discontinuities in the uncertainties are due to replacement of one sample with another and with adjustments made to the ion-chamber electronics settings at 41, 35, 30, 25, 21.8, and 20.8 keV. These adjustments change the noise level associated with the ion chambers, but the continuity of the measured attenuations (Fig. 3) shows that the normalization procedure prevents these adjustments from having any significant impact on the measured attenuations.

B. A full-foil absolute measurement of the mass attenuation coefficient

In this section we summarize our use of a full-foil x-ray mapping technique to determine the mass attenuation coefficient of the thickest foil at the highest available energy to high accuracy [31]. We determine an *attenuation profile* of the foil plus holder $([\mu/\rho][\rho t]_{xy})_{F+H}$ by performing a raster measurement of the attenuation at (x, y) locations across the entire foil mounted in the holder. We determine the relatively small holder contribution to the attenuation profile by use of a fitting routine. The determined holder contribution was less
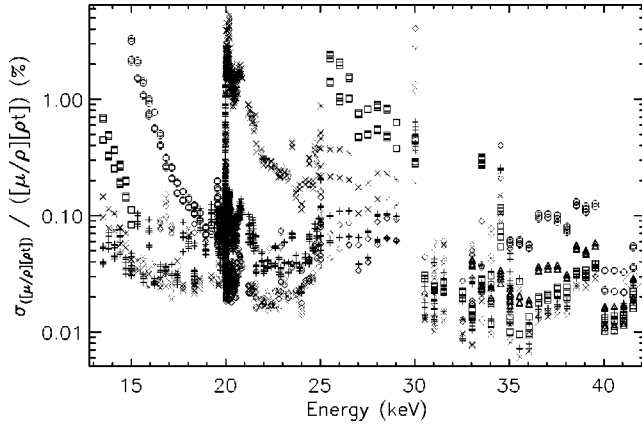
FIG. 4. Percentage uncertainties in the measured attenuations following Eq. (5). Note that despite a consistent approach to the data acquisition, some measurements have (statistical) uncertainties exceeding 1%, due to the foil thickness. However, in each case other foils of more optimum thickness measured at the same energies have uncertainties of 0.006–0.03 %, so that the final results are not compromised by the "poor" data. The results of measurements obtained using the two downstream ionization chambers with variously sized apertures placed between the absorber and the ionization chamber, that cannot be resolved in Fig. 3, are clearly resolved here. Foil markers as for Fig. 3. The points marked by the large diamonds ($\diamondsuit$) at 41.5 keV (unresolved) are discussed in Sec. III B.

than 5% of the foil attenuation. Subtraction of the fitted holder profile from the total measured profile then produces an attenuation profile of the foil, $([\mu/\rho][\rho t]_{xy})_F$.

The average of the attenuation profile measured at a number of (x,y) locations across the entire foil is related to the average integrated column density $\overline{[\rho t]}$ of the foil by

$$\overline{\left(\left[\frac{\mu}{\rho}\right][\rho t]_{xy}\right)_F} = \left[\frac{\mu}{\rho}\right]\overline{[\rho t]_{xy}} = \left[\frac{\mu}{\rho}\right]\overline{[\rho t]} = \left[\frac{\mu}{\rho}\right]\frac{m}{A}, \quad (6)$$

so that

$$\left[\frac{\mu}{\rho}\right] = \frac{A}{m}\overline{\left(\left[\frac{\mu}{\rho}\right][\rho t]_{xy}\right)_F}, \quad (7)$$

yielding a precise and absolute value of the mass attenuation coefficient. By this method we determine $[\mu/\rho]$ to be 11.6514±0.0063 cm^2/g and 11.6582±0.0032 cm^2/g, using the counts recorded in the first and second of the downstream ion chambers. These results are consistent within their associated measurement and fitting uncertainties. The absolute results determined by this technique are represented in the figures by the large diamond markers ($\diamondsuit$). Further details of the technique are discussed in [31].

We did not use the full-foil x-ray mapping technique to determine the mass attenuation coefficient at each energy as this would have been too time consuming.

C. Scaling other mass attenuation coefficients

If the other measured attenuations are divided by the average integrated column density $\overline{[\rho t]}=m/A$ of the relevant foil, this results in systematic differences of up to 2% between the mass attenuation coefficients measured at the same energy with different foils. Our work with full-foil measurements indicates that a difference of this magnitude could easily result from foil nonuniformities which this averaging procedure neglects [10,23,31].

We have the beam passing through the same point of the foil for all measurements for which that foil was used, so that the integrated column density of the foil is common for all measurements made with a given foil. The measurements were therefore scaled by varying the integrated column density of each of the foils according to

$$\left[\frac{\mu}{\rho}\right] \rightarrow \left[\frac{\mu}{\rho}\right]' = \frac{[\mu/\rho]\overline{[\rho t]}}{[\rho t]_T}, \quad (8)$$

where $[\rho t]_T$ is the trial value of the integrated column density of the foil. We used a fitting routine to vary $[\rho t]_T$ until the difference between the mass attenuation coefficients was minimized. The minimized parameter is

$$\chi^2 = \sum_{E_i}\sum_{F_j}\left(\frac{[\mu/\rho]'_{E_iF_j} - \overline{[\mu/\rho]'_{E_i}}}{\sigma([\mu/\rho]_{E_iF_j})}\right)^2, \quad (9)$$

which is defined by analogy with the χ^2 measure of deviations. The summations in Eq. (9) cover measurements obtained at all energies E_i using all measured foils F_j. The term in the parentheses is the difference between the (scaled) value obtained using the foil F_j at energy E_i, $[\mu/\rho]'_{E_iF_j}$, and the weighted mean of the scaled values obtained at energy E_i, $\overline{[\mu/\rho]_{E_i}}$, divided by the measurement uncertainty $\sigma([\mu/\rho]_{E_iF_j})$. The full-foil absolute value is included in the evaluation of χ^2 but, of course, not varied. Minimization of χ^2 optimizes the weighted agreement between the results determined using each of the foils and the absolute value at the full-foil mapping energy and also the weighted agreement of the relative measurements. The scaling is based on an iterative least-squares minimization of the difference between the results.

The physical removal and replacement of a foil in the sample stage generally results in the presentation of a slightly different part of the foil to the beam. We estimate that this replacement shifts the location of the beam footprint on the foil by less than around 300 μm. This shift has the effect that the integrated column density of the local region of the foil may be significantly different for the two placements. In the scaling procedure nine integrated column densities relating to seven foils have therefore been varied to minimize the discrepancies between 5161 measurements at 527 energies.

The mass attenuation coefficients are evaluated as the weighted mean of the measurements obtained with all foil and aperture combinations at each energy. We examine the consistency of the scaled values in Fig. 5 where we present the percentage difference of the measurements for each foil from the weighted mean at each energy. The unresolved large diamond markers ($\diamondsuit$) represent the results of the absolute measurements described in Sec. III B. In this figure we can see a number of prominent divergences from the zero line.
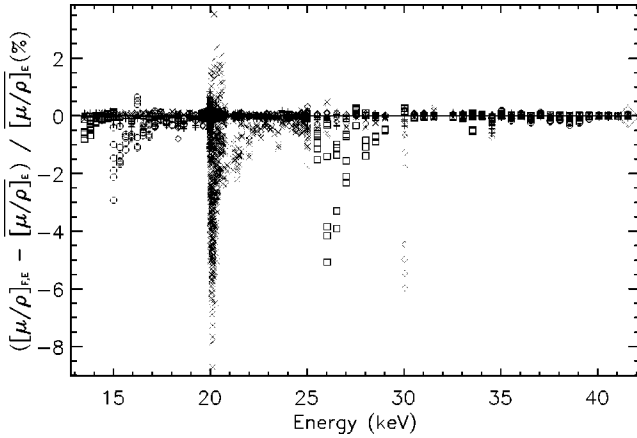
FIG. 5. Percentage difference of the measured values from the weighted mean at each energy after scaling. A number of divergences have become apparent. These divergences correlate with increasing thickness of the foil used to make the measurement. The markers represent results obtained using foils of the following nominal thicknesses: $\diamond$, 25 μm; +, 50 μm; ×, 100 μm; $\square$, 150 μm; $\triangle$, 200 μm; $\bigcirc$, 250 μm; $\diamondsuit$, full-foil measurement.

These include two inconsistencies, at 30 and 35 keV, which are readily distinguished from systematic trends by virtue of their transience, and a prominent complex of deviations occurring around the absorption edge at 20 keV. Four further systematic divergences can be seen, where the measured value obtained using one of the foils diverges systematically below the zero line. These divergences fall to around 4% below the zero line at 25 keV ($\square$ marker), 2–4 % below at 20 keV (× marker), 2% below at 15 keV ($\bigcirc$ marker), and 0.8% below at 13.5 keV ($\square$ marker). Comparison with Fig. 3 shows that these divergences correlate with rising foil attenuations. The onset of the divergence typically occurs when the foil attenuation increases above 4–5.

We have assessed the accuracy of the scaling procedure by comparing the fitted integrated column densities against their measured average values determined in Sec. II A. Assuming that the variation of the integrated column density across the foil is random, the fitted and average integrated column densities should, on average, be in agreement. On average the fitted integrated column densities are 1.2 standard deviations below the measured average values, where the standard deviation is evaluated as the quadrature sum of the fitting and measurement uncertainties. As the spread in the differences between the fitted and measured integrated column densities is 1.6 standard deviations, these results are consistent within the observed variation.

A quantitative measure of the improvement in the consistency of the measured values is also gained from the reduction of the reduced χ_r^2 (χ^2 per degree of freedom). Without scaling (using $\overline{[\rho t]}$) the measurements obtained using different foils differed by up to 2% due to local thickness variations yielding a large χ_r^2 of 114. After scaling this χ_r^2 is dramatically reduced to 3.94, reflecting the high degree of consistency of the scaled values across all of the parameter space but especially across the extended energy range.

The statistical significance of the discrepancies presented in Fig. 5 can be appreciated by comparing the magnitudes of
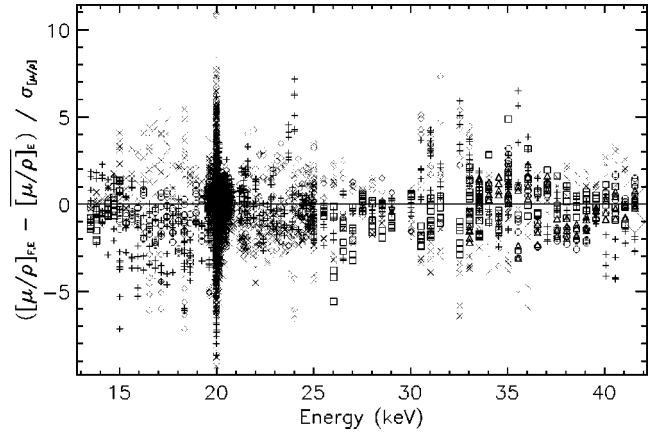
FIG. 6. Significance of deviations from weighted mean, after scaling. Significance is defined in Eq. (10). Symbols as for Fig. 3. Significant outliers are seen in the near-edge region, implying the existence of uncorrected systematics such as the bandwidth effect (see Appendix A 1).

the discrepancies with the measurement uncertainties. In Fig. 6 we present the significance of the deviations from the weighted mean, defined as

$$\text{significance} = \frac{[\mu/\rho]_{E_i F_j} - \overline{[\mu/\rho]_{E_i}}}{\sigma([\mu/\rho]_{E_i F_j})}. \qquad (10)$$

As can be seen from a comparison with Eq. (9), the significance describes contributions to χ_r^2. In Fig. 6 we can see that the significance of the four regions of large divergence shown in Fig. 5 is generally very low, reflecting the low statistical precision associated with these measurements. Thus, while the divergences represent real systematic deviations in the results, they fall within the experimental uncertainty and do not exert significant influence on the weighted mean of the measurements. The persistence of the prominent complex of discrepancies about the absorption edge in Fig. 5 indicates their statistical significance.

D. Other systematic effects

Numerous other key systematics must be dealt with in this paper, in order to achieve the accuracies claimed below. In several cases these required techniques and approaches not elsewhere discussed. We therefore present these in the Appendix in order to avoid distracting attention from the major conclusions, but allowing the reader to follow these details as they see fit.

IV. CALIBRATION OF X-RAY PHOTON ENERGIES

The photon energy was directly determined by diffraction from a germanium crystal mounted on a Huber four-circle diffractometer as depicted in Fig. 2. With the attenuating samples out of the x-ray beam, foils mounted on the daisy wheel were introduced into the beam path to decrease the intensity of the x-ray beam used to measure the rocking curves.
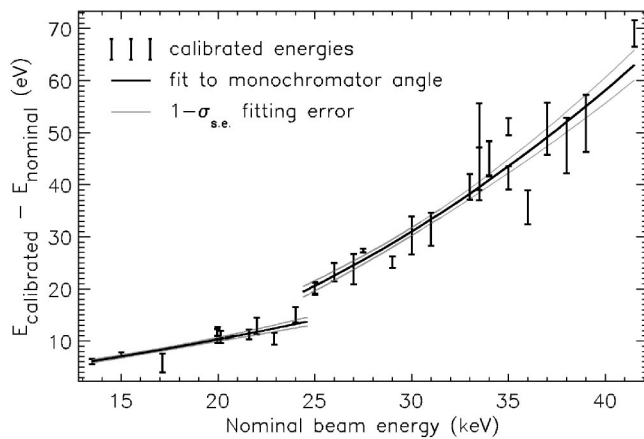
FIG. 7. Results of the energy calibration process. A series of (hhh) peaks was measured at a number of energies. These were used to determine the x-ray energy, represented here by the error bars. These energies were fitted to the monochromator crystal angle by Eq. (11), and this fitted function was used to interpolate the x-ray energy from the monochromator angle for all measurements. The results of this fitting process and the interpolation are shown here by the line of best fit (heavy, black) and the uncertainty (light, gray), estimated from the covariant error matrix returned by the fitting program.

Rocking curves were recorded with the x-ray intensity reflected into a stationary sodium iodide scintillation detector whose face was centered on the predicted Bragg angle of the reflection. The detector used was "wide open," with no further angular selection applied to the reflected beam. The germanium crystal was rotated through a small range of angles about the Bragg angle to record the rocking curve of the reflection. Between three and thirteen such rocking curves were recorded at each directly measured energy, diffracted by lattice planes of the form (hhh) with h ranging from 1 up to 17. The angular locations of these rocking curves were determined by fitting with a Lorentzian and also by determining their centers of mass. Two independent techniques for determining the angular locations were employed to avoid the effects of the saturation of the detector used to measure the diffracted intensities.

The largest single source of systematic error in the energy determined in this manner is due to the misalignment of the zero-angle position of the germanium crystal. We have corrected for this source of error using an adaptation of a standard technique [32]. Extrapolation of a plot of $a_0 \sin \theta_{hkl}/\sqrt{h^2+k^2+l^2}$ versus $a_0 \cos \theta_{hkl}/\sqrt{h^2+k^2+l^2}$ to the limit $\cos \theta_{hkl}=0$ allows one to determine the energy of the beam from the $\sin \theta_{hkl}$ intercept, as well as the magnitude of the zero-angle misalignment of the germanium crystal. The lattice parameter of germanium was taken to be $a_0 = 5.657\,82$ Å [33].

The determined energies, depicted as points with error bars in Fig. 7, were used to calibrate the x-ray energy across the entire measurement range. This was achieved by fitting a modified Bragg function which related the monochromator angle to the directly determined energies. The fitting function used was

$$E = \frac{hc\sqrt{h^2 + k^2 + l^2}}{2a_0(1 + \delta_{a_0})\sin(\theta + \delta_\theta)}, \qquad (11)$$

which follows directly from Bragg's law, with a small adjustment to the monochromator lattice parameter via the parameter δ_{a_0}, allowing for an expansion of the crystal due to the x-ray heat load; and an offset angle δ_θ of the monochromator crystal, which allows for mechanical slack in the crystal rotation stage and errors in the crystal alignment. We have used values for hc and the lattice parameter for silicon taken from Ref. [34]. Diffraction was from the $(hkl)=(3,1,1)$ planes of the silicon monochromator.

The monochromator angles were fitted separately over two energy ranges corresponding to the change from the fifth to the third undulator harmonic at about 25 keV, possibly resulting in a change in the value of the lattice parameter δ_{a_0} due to the different heat load. In Fig. 7 we show the results of this process, where the abscissa is the nominal synchrotron x-ray energy and the ordinate is the difference between the calibrated and nominal energies. The error bars represent the directly determined energies and the solid lines are the best fits to these energies, determined using Eq. (11). The gray lines above and below the fitted energies are the error estimates evaluated from the covariant error matrix returned from the fitting procedure. By this procedure the x-ray energies have been determined to a precision of between 0.0015% and 0.007% across the entire measurement range.

The directly determined energies are generally consistent with the smoothly interpolated fit with a few points indicating a possible additional small variation of the beam energy not correlated with the monochromator angle. Accordingly we use the smoothly interpolated values.

The accuracy of the energy determination can be assessed by comparing the absorption edge energy against its most accurate literature value. The first point of inflection of the mass attenuation coefficient on the absorption edge occurs at $19.9944 \pm 0.0002 \pm 0.0003$ keV, where the first uncertainty reflects our ability to locate the position of the point of inflection and the second is our uncertainty in determining the energy. Comparison with the result of Ref. [35], $20.000\,36 \pm 0.000\,02$ keV, indicates a discrepancy of 6 eV or 0.03%. The most likely cause of this discrepancy is a difference in the interpretation of the absorption-edge location, chemical or thermal effects on the edge location, or further errors in the energy determination. We consider an upper limit on the accuracy of our determined energies to be half of the difference between these absorption-edge locations at about 0.015%.

V. TABULATION OF THE RESULTS

In Table I we present the values of the mass attenuation coefficients measured at 101 energies between 13.5 and 41.5 keV. A further 425 measurements made at energies between 19.560 and 21.452 keV are not detailed here due to space limitations. The complete tabulation of measured values is available electronically [42]. In the first column we present the calibrated photon energy (in keV) with the uncertainty in the last significant figures presented in parentheses.

TABLE I. Mass attenuation coefficients $[\mu/\rho]$ and the imaginary component of the atomic form factor f_2 as a function of x-ray energy, with one standard deviation uncertainties in the least significant digits indicated in parentheses. We present also the percentage uncertainty in the mass attenuation coefficients $\sigma_{[\mu/\rho]}/[\mu/\rho]$. Uncertainty in f_2 includes the measurement uncertainty and the difference between major tabulations of the total Rayleigh plus Compton scattering cross sections. Values of f_2 in the energy range of 19.9-20.9 keV are likely to be affected by solid-state and atomic effects. A further uncertainty, of the same order as the XAFS amplitude, may apply to these values when alternate atomic environments are investigated. The complete tabulation of measured values is available electronically [42].

Energy (keV)	$[\mu/\rho]$ (cm^2/g)	$\sigma_{[\mu/\rho]}/[\mu/\rho]$	f_2 (e/atom)	Energy (keV)	$[\mu/\rho]$ (cm^2/g)	$\sigma_{[\mu/\rho]}/[\mu/\rho]$	f_2 (e/atom)
13.50614(31)	37.868(25)	0.067%	1.1125(17)	21.39129(49)	69.804(42)	0.060%	3.3539(31)
13.80632(31)	35.596(35)	0.098%	1.0671(18)	21.47137(49)	69.034(35)	0.050%	3.3289(30)
14.10651(30)	33.578(24)	0.070%	1.0267(14)	21.49137(50)	68.899(40)	0.058%	3.3254(31)
14.40668(30)	31.615(23)	0.072%	0.9855(11)	21.59145(51)	67.990(22)	0.032%	3.2964(28)
14.70686(29)	29.860(18)	0.060%	0.94861(79)	21.61144(51)	67.725(39)	0.057%	3.2864(32)
15.00705(29)	28.193(30)	0.11%	0.9123(11)	21.91170(53)	65.204(32)	0.048%	3.2069(33)
15.33725(28)	26.552(16)	0.060%	0.87656(70)	22.01178(54)	64.377(30)	0.046%	3.1802(33)
15.63743(28)	25.147(18)	0.071%	0.8451(11)	22.21189(56)	62.777(26)	0.042%	3.1286(34)
15.93764(27)	23.840(26)	0.11%	0.8152(17)	22.31196(57)	62.025(19)	0.030%	3.1047(33)
16.23781(27)	22.627(15)	0.065%	0.7869(20)	22.41206(58)	61.285(28)	0.046%	3.0811(35)
16.53801(27)	21.493(24)	0.11%	0.7600(25)	22.61217(60)	59.807(25)	0.041%	3.0329(35)
16.83818(27)	20.405(21)	0.10%	0.7333(28)	22.81234(62)	58.415(19)	0.033%	2.9878(35)
17.13837(27)	19.448(21)	0.11%	0.7101(30)	22.91241(64)	57.729(27)	0.047%	2.9653(36)
17.43858(28)	18.494(17)	0.091%	0.6857(31)	23.11257(66)	56.412(32)	0.057%	2.9224(37)
17.73878(28)	17.640(11)	0.064%	0.6640(31)	23.31273(68)	55.107(29)	0.053%	2.8788(36)
18.03897(29)	16.825(19)	0.11%	0.6427(33)	23.51287(70)	53.980(45)	0.084%	2.8437(41)
18.33920(30)	16.073(18)	0.11%	0.6229(33)	23.71305(72)	52.635(39)	0.074%	2.7957(38)
18.63937(31)	15.350(16)	0.11%	0.6032(31)	23.91316(75)	51.469(20)	0.038%	2.7563(33)
18.93958(32)	14.6337(95)	0.065%	0.5828(27)	24.01324(76)	50.763(43)	0.085%	2.7294(39)
19.23980(34)	14.0142(95)	0.068%	0.5655(22)	24.21342(78)	49.785(25)	0.050%	2.6987(33)
19.54001(35)	13.3834(92)	0.069%	0.5469(18)	24.41356(81)	48.691(24)	0.049%	2.6606(32)
19.62006(36)	13.236(14)	0.10%	0.5427(16)	24.4195(10)	48.769(24)	0.050%	2.6656(32)
19.70011(36)	13.105(11)	0.085%	0.5392(14)	24.61370(83)	47.643(21)	0.043%	2.6242(31)
19.78018(37)	12.9752(41)	0.032%	0.5356(11)	24.72002(99)	47.224(46)	0.096%	2.6122(38)
19.84023(37)	12.9142(35)	0.027%	0.53461(99)	24.82026(99)	46.665(29)	0.062%	2.5914(32)
19.92027(37)	13.0489(94)	0.072%	0.54301(88)	24.92046(98)	46.217(21)	0.045%	2.5767(29)
19.97382(38)	14.3735(28)	0.020%	0.60487(63)	25.02061(97)	45.770(54)	0.12%	2.5618(40)
19.99233(38)	24.407(32)	0.13%	1.0628(16)	25.52154(94)	43.411(38)	0.088%	2.4772(32)
20.00032(38)	53.827(44)	0.081%	2.4048(21)	26.02257(90)	41.216(73)	0.18%	2.3970(47)
20.01033(38)	90.997(28)	0.031%	4.1017(14)	26.52354(87)	39.167(59)	0.15%	2.3204(39)
20.10991(39)	86.245(68)	0.078%	3.9044(31)	27.02457(84)	37.244(30)	0.080%	2.2471(22)
20.20496(39)	81.042(14)	0.017%	3.68334(63)	27.52557(81)	35.478(31)	0.089%	2.1792(21)
20.29850(40)	79.243(36)	0.046%	3.6173(17)	28.02663(79)	33.794(32)	0.096%	2.1124(21)
20.39659(41)	79.902(40)	0.050%	3.6656(19)	28.52764(77)	32.240(25)	0.078%	2.0503(16)
20.49469(41)	79.411(43)	0.054%	3.6605(21)	29.02876(76)	30.766(13)	0.042%	1.98985(86)
20.58672(42)	79.605(33)	0.041%	3.6862(18)	30.03102(76)	28.06(11)	0.40%	1.8757(77)
20.66679(43)	77.677(27)	0.034%	3.6098(17)	30.53217(78)	26.840(16)	0.061%	1.8228(13)
20.74685(43)	76.413(24)	0.032%	3.5642(17)	31.03332(80)	25.690(13)	0.052%	1.7723(12)
20.83088(44)	76.01(13)	0.17%	3.5595(63)	31.53462(84)	24.603(14)	0.058%	1.7236(13)
20.87093(44)	75.069(31)	0.041%	3.5217(21)	32.53700(94)	22.622(14)	0.064%	1.6332(13)
21.19114(47)	71.733(24)	0.033%	3.4153(23)	33.0383(10)	21.6995(84)	0.039%	1.58968(99)
21.27123(48)	70.970(37)	0.052%	3.3914(28)	33.5396(11)	20.8372(93)	0.044%	1.5487(10)
21.29125(48)	70.740(34)	0.048%	3.3834(27)	34.0409(11)	20.0205(63)	0.032%	1.50923(92)

TABLE I.   (*Continued.*)

Energy (keV)	$[\mu/\rho]$ (cm²/g)	$\sigma_{[\mu/\rho]}/[\mu/\rho]$	f_2 (e/atom)	Energy (keV)	$[\mu/\rho]$ (cm²/g)	$\sigma_{[\mu/\rho]}/[\mu/\rho]$	f_2 (e/atom)
34.5423(12)	19.227(17)	0.090%	1.4697(15)	38.5535(21)	14.2930(67)	0.047%	1.21244(61)
35.0435(13)	18.5140(68)	0.037%	1.43478(81)	39.0551(22)	13.8009(57)	0.042%	1.18506(52)
35.5449(14)	17.8122(68)	0.038%	1.39917(77)	39.5566(23)	13.3374(40)	0.030%	1.15908(36)
36.0463(15)	17.1566(54)	0.031%	1.36574(66)	40.0581(25)	12.8838(28)	0.022%	1.13294(27)
36.5478(16)	16.5205(44)	0.026%	1.33242(54)	40.5598(26)	12.4559(32)	0.026%	1.10821(30)
37.0492(17)	15.9303(39)	0.025%	1.30151(46)	41.0614(28)	12.0437(22)	0.018%	1.08396(21)
37.5505(18)	15.3534(42)	0.027%	1.27039(43)	41.5630(29)	11.6535(29)	0.025%	1.06082(28)
38.0521(20)	14.8120(43)	0.029%	1.24104(41)				

In the second column we present the mass attenuation coefficient $[\mu/\rho]$ (in cm²/g) with its uncertainty. In the third column we present as an aid to the reader the percentage uncertainty in the mass attenuation coefficient. The values in the second and third columns have been determined from the weighted mean of the measurements made with a variety of apertures and foil thicknesses, and using the values determined from the counts recorded in both of the downstream ion chambers. The weighted mean typically involves between 18 and 30 determinations. The uncertainty in the mass attenuation coefficient was evaluated from σ_{sd} defined in Eq. (A3). The measured mass attenuation coefficients are plotted as a function of energy in Figs. 8 and 9.

In the fourth column of Table I we present the imaginary component of the atomic form factor f_2, evaluated from

$$f_2 = \frac{EuA[\mu/\rho]_{pe}}{2hcr_e}, \qquad (12)$$

where E is the photon energy in eV, u is the atomic mass unit, A is the relative atomic mass of molybdenum, h is the Planck constant, c is the speed of light, r_e is the classical electron radius, and $[\mu/\rho]_{pe}$ is the photoelectric component of the attenuation. $[\mu/\rho]_{pe}$ has been evaluated by subtracting the average of the Rayleigh plus Compton contributions as tabulated in XCOM [16,17] and FFAST [11–13]. In parentheses

following the reported values is the uncertainty in f_2, evaluated from

$$\sigma_{f_2} = \frac{EuA}{2hcr_e}(\sigma_{[\mu/\rho]}^2 + \Delta_{RC}^2)^{1/2}, \qquad (13)$$

which includes an uncertainty contribution of half of the difference Δ_{RC} between the tabulated values of the Rayleigh plus Compton contributions.

The use of the photoelectric component of the attenuation determined in this manner is appropriate when Rayleigh and Compton scattering are the only significant other contributions to the total attenuation. This is certainly the case in the energy range covered by this experiment except near the absorption edge and in the region of the XAFS. In these regions the influence of solid-state and bonding effects is difficult to calculate. It may well be that values of f_2 in the energy range from 19.9 to 20.9 keV should be subject to a further uncertainty, of the same order as the XAFS amplitude, when alternate atomic environments are investigated. Estimates of the individual error contributions to the reported values are presented in Table II.
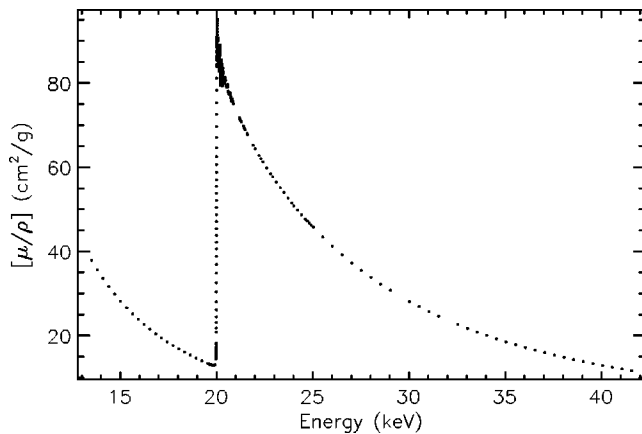
FIG. 8. Energy dependence of the measured mass attenuation coefficients.
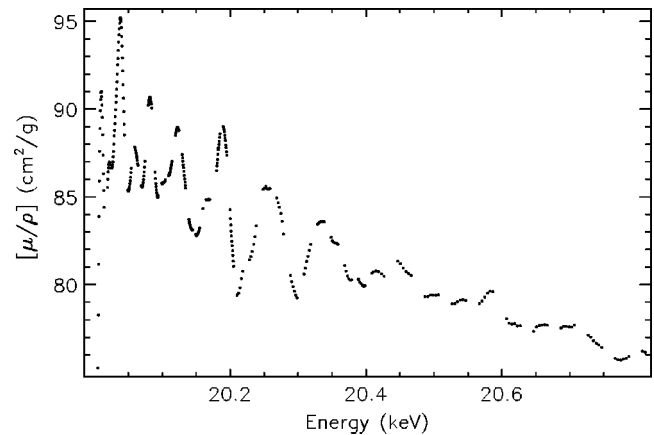
FIG. 9. Detail of the measured mass attenuation coefficients in the region of the XAFS. Marker size corresponds approximately to the measurement uncertainty.

TABLE II. Error contributions to the values reported in Table I, with source specified. Further established limits for the systematic uncertainty are quoted here.

Quantity	Estimated magnitude	Contributions and comments	
		Away from the absorption edge	
$[\mu/\rho]$	0.028%	Accuracy limited by the full-foil mapping technique (Sec. III B)	
	0.02-0.15 %	Precision, limited by counting statistics and foil replacement errors	
	<0.03%	Unidentified systematic component: one-quarter of correction (Appendix A 2 e)	
		Near the absorption edge (19.99−21 keV)	
$[\mu/\rho]$	0.01-0.06 %	X-ray bandwidth (Appendix A 1)	Total accuracy near edge
	0.003-0.006 %	Sample roughness (Appendix A 2 c)	0.03-0.1 %
	<0.01%	Harmonic components (Appendix A 2 b)	
	0.005-0.01 %	Secondary photons (Appendix A 2 a)	
E	0.0015-0.007 %	Accuracy of monochromator dispersion function interpolation (Sec. IV)	
f_2	0-0.2-0.5 %	Inconsistency of subtracted scattering components (Sec. V)	

VI. COMPARISON WITH TABULATED VALUES OF THE PHOTOELECTRIC ABSORPTION COEFFICIENT $[\mu/\rho]_{\rm pe}$

The mass attenuation coefficient can be written as a sum of photoelectric absorption $[\mu/\rho]_{\rm pe}$, Rayleigh scattering $[\mu/\rho]_R$, and Compton scattering $[\mu/\rho]_C$ according to

$$\left[\frac{\mu}{\rho}\right] \approx \left[\frac{\mu}{\rho}\right]_{\rm pe} + \left[\frac{\mu}{\rho}\right]_R + \left[\frac{\mu}{\rho}\right]_C. \qquad (14)$$

We do not include further attenuating processes in this summation as they are negligible in the energy region of this experiment.

The results of atomic form-factor calculations can be assessed by comparing the calculated photoelectric absorption coefficients with our measured values. Note that we have not directly measured the Rayleigh and Compton crosssections, but instead estimate the Rayleigh plus Compton cross section to be equal to the average of the values reported by the FFAST and XCOM tabulations. We estimate the uncertainty in the Rayleigh plus Compton cross section to be half of the difference between these tabulations. We have subtracted these scattering components from the measured values to determine photoelectric absorption coefficients.

In Fig. 10 we present the percentage discrepancy between a variety of commonly used tabulations of $[\mu/\rho]_{\rm pe}$ and our results. Our experimental results form the zero (reference) line, with the measurement uncertainties presented as error bars about this zero line. The uncertainty in the subtracted Rayleigh plus Compton cross-sections is presented as a shaded region around the zero line. Except in the region immediately below the absorption edge the uncertainty in the subtracted Rayleigh plus Compton cross-sections is generally less than our experimental error-bars.

Figure 10 shows that the XCOM calculation exhibits a large difference from the measured values over an extended range of energies above the absorption edge. There is some evidence of an oscillatory behavior in the XCOM values, possibly extending beyond the measured energy range. Oscillatory behavior in the calculated values has been observed

elsewhere [11,12] and may be the result of an incompletely converged calculation. The FFAST tabulation is in best agreement with the measurements.

The difference between the various calculations and our results in the below-edge region are remarkably similar in form, even though they differ by 4–5 % in the absolute level of the photoelectric absorption coefficient. The similarity of these differences may imply a common limitation of the calculations in this region. At the point immediately below the absorption edge the FFAST calculation is in best agreement with our photoelectric absorption coefficient.

Previous highly accurate measurements for copper [1] and silver [39] have reported a similar difference between the measured values and the FFAST tabulation in the region immediately above the absorption edge, extending out to approximately 25% of the absorption-edge energy. Over this region the measured values typically decrease from being 3–5 % higher than the FFAST values to around the level of the FFAST values. This difference is again observed in the results for molybdenum, as can be seen in Fig. 10. The presence of this effect in three elements indicates either a systematic problem with the FFAST formalism or the presence of an unrecognized contribution to the measured attenuation in this region.

A further systematic difference between the measured values and the FFAST tabulation, similar to that observed in silver [39], is observed below the absorption edge. In the case of silver the FFAST tabulation is approximately 2.5% below the measured values at energies well below the absorption edge. This difference begins to decrease at about 5 keV below the absorption edge, converging to the measured value immediately below the absorption edge. Such a pattern of systematic differences is also observed for molybdenum and may provide further insight into the limitations of the FFAST formalism.

VII. CONCLUSION

We have determined the mass attenuation coefficients of molybdenum on an absolute scale. The measurements are
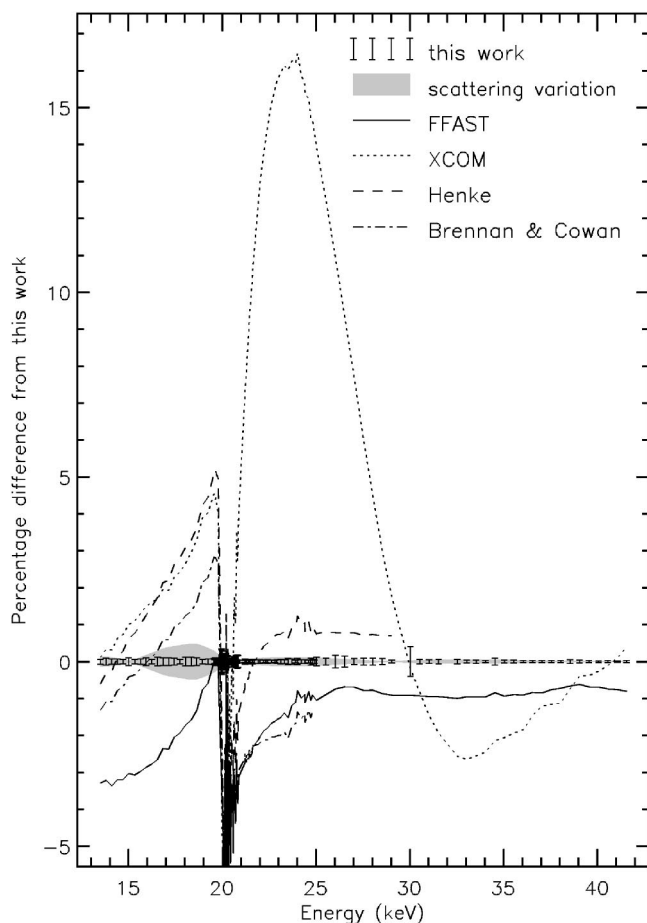
FIG. 10. Percentage discrepancy between various tabulated values of $[\mu/\rho]_{pe}$ and this work. We have determined $[\mu/\rho]_{pe}$ by subtracting the average of the calculated Rayleigh plus Compton scattering cross sections of FFAST and XCOM from our measured values. The results of this work appear along the zero line, with error bars reflecting the experimental uncertainties. The narrow gray region around the zero line represents half of the difference between the Rayleigh plus Compton scattering cross sections tabulated in XCOM and FFAST, and reflects the likely error in the absorption coefficient evaluated using these different models. Tabulated values are taken from FFAST [11–13], XCOM [16,17], Henke *et al.* [36], and Brennan and Cowan [37,38].

placed on an absolute scale by comparison with the results of a full-foil mapping procedure which has been used to determine the mass attenuation coefficient at a single energy.

Measurements have been made over an extended range of the measurement parameter space. The values obtained from this extended investigation have been examined for the effect of systematic errors on the measurement. We have corrected a systematic error in the measured values arising from the effect of the bandwidth of the x-ray beam used to make the measurement (whose effect is particularly pronounced along the rise of the absorption edge). A small residual deviation in the measurements is consistent with an incorrectly determined dark current, and corrected as such.

The measurements are compared with a variety of predictions of the photoelectric absorption coefficients. Some of the available tabulations are in very poor agreement with the results of this work. The FFAST tabulation is in best agreement with our set of measurements, with discrepancies of about 1% far above the absorption edge and up to 4% near and below the absorption edge.

Systematic differences between the FFAST calculation and the results of a number of recent experiments are confirmed for molybdenum. The systematic nature of these differences indicates that the FFAST calculation needs to be refined in certain regions, in particular immediately below and above the *K*-shell absorption edge. These discrepancies may indicate new physics, particularly in the above-edge region.

Absolute measurements in the near-edge region will be of interest in solid-state and bonding studies, and in particular for those wishing to compute XAFS and XANES on an absolute scale.

ACKNOWLEDGMENTS

APPENDIX: DETERMINING THE MASS ATTENUATION COEFFICIENT: OTHER SYSTEMATIC EFFECTS

1. The x-ray bandwidth

We have shown elsewhere that the discrepancies between measurements on the absorption edge are correlated with the gradient of the mass attenuation coefficient, and that this correlation is due to the energy bandwidth of the x-ray beam [40]. The bandwidth effect arises from the energy dependence of the mass attenuation coefficient, so that the different spectral components of the x-ray beam are attenuated to varying degrees by the absorber. As the beam penetrates the absorber this differential attenuation modifies the beam energy profile such that the intensities of the lesser attenuated components gradually increase relative to those of the more attenuated components.

This modification of the beam energy profile leads to the systematic decrease of the measured mass attenuation coefficient with increasing thickness of the attenuating foil. In [40] a particularly sensitive subset of measurements around the absorption edge was used to determine the bandwidth of the synchrotron beam to be 1.57±0.03 eV at 20 keV.

Away from absorption edges the mass attenuation coefficient varies sufficiently slowly for the bandwidth effect to be insignificant. However, on the absorption edge and in the region of the XAFS, where the mass attenuation coefficient changes rapidly as a function of energy, the effect of the bandwidth is significant. This effect has obviously contributed to the discrepancies at around 20 keV in Figs. 5 and 6.
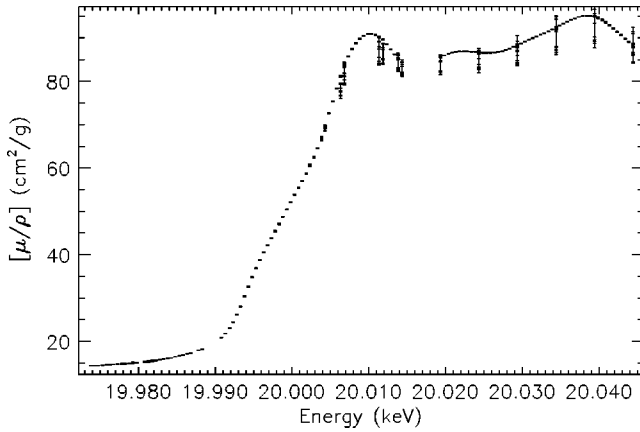
FIG. 11. Mass attenuation coefficients in the neighborhood of the absorption edge and the XAFS. The values on the absorption edge can be linearized in order to correct for the effect of the bandwidth of the x-ray beam. Points are marked by their σ_{se} error bars.

When the change in the mass attenuation coefficient over the scale of the bandwidth of the x-ray beam is approximately linear, its effect can be corrected by following [40]

$$\left[\frac{\mu}{\rho}\right] \rightarrow \left[\frac{\mu}{\rho}\right]' = \left[\frac{\mu}{\rho}\right] + \frac{1}{[\rho t]} \ln\left[\sum_{k=-j}^{j} \tilde{I}_0(E_0 + k\Delta E)\right.$$

$$\left. \times \exp\left(-\frac{d[\mu/\rho]_{E_0}}{dE}(k\Delta E)[\rho t]\right)\right], \qquad (A1a)$$

$$j = \frac{r_W(s_{FWHM} - 1)}{2}, \quad \Delta E = \frac{W_{FWHM}}{s_{FWHM} - 1}, \qquad (A1b)$$

where $\tilde{I}_0$ is the incident beam energy profile, representing the distribution of energies within the beam about the central energy E_0. $d[\mu/\rho]_{E_0}/dE$ is the energy derivative of the weighted mean of the mass attenuation coefficients at the central energy. The summation is evaluated over a range of energies corresponding to r_W times the full width at half maximum (FWHM) of the bandwidth and is discretely sampled s_{FWHM} times per FWHM bandwidth. Here we use $r_W = 10$ and $s_{FWHM} = 9$ [40].

In Fig. 11 we present the results of measurements made along the absorption edge and within the first few XAFS oscillations. Along the rise of the absorption edge the gradient of the mass attenuation coefficient reaches its maximum value and the bandwidth effect is greatest. Furthermore, along this rise the mass attenuation coefficient is approximately linear on the scale of the bandwidth of the beam (1.57 eV [40]). However, the mass attenuation coefficient is not linear on the scale of the bandwidth of the beam at around 20.01 keV, where the mass attenuation coefficient reaches its first (and most strongly curved) maximum.

We have included a correction for the bandwidth effect [Eq. (A1)] in the fitting routine. We now fit the FWHM bandwidth of the beam W_{FWHM} (with appropriate allowance for the energy dependence of the bandwidth), and scale the nine integrated column densities as before to minimize the χ^2 dif-
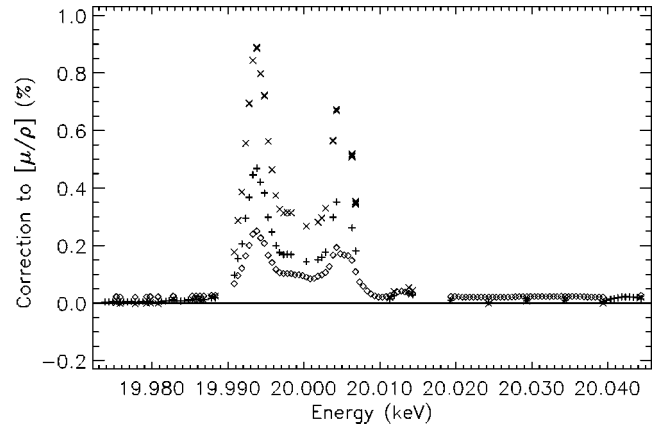
FIG. 12. Correction to the mass attenuation coefficients measured in the neighborhood of the absorption edge and in the region of the XAFS, evaluated using the linearized approximation for the bandwidth. The correction in the XAFS region is everywhere less than 0.03%, indicating that the correction resulting from this approximation is at the level of the experimental uncertainties. Symbols as for Fig. 3.

ferences between the measurements at each energy. In Fig. 12 we present the results of this fitting in the form of the correction applied to the mass attenuation coefficients measured on the absorption edge. From this figure we see that the correction for the bandwidth effect is correlated with the gradient of the mass attenuation coefficient and increases with the thickness of the foil used to make the measurement. The baseline value for each of the foils differs slightly from zero due to a further small adjustment to the scale of the integrated column densities.

The linearization adopted in [40] is valid when the variation of the mass attenuation coefficient on the scale of the bandwidth of the beam is approximately linear. Alternate Fourier deconvolution techniques for correcting the bandwidth effect encounter other difficulties preventing their simple application, as discussed in [40]. We have also compared the linearized and the Fourier-deconvolution techniques in the region of the XAFS and have found that the linearized approach is quite adequate for addressing the effect of the bandwidth on these measurements.

We estimate the effect of the bandwidth in regions where the linearized approach may fail, i.e., at the extrema of the XAFS. We observe that the effect of the bandwidth at these extrema is less than twice that predicted by the linearized model—due to the two-sided nature of the extremum—when the gradient is taken to be the maximum gradient within the energy span of the beam. We take this energy span to be equal to twice the FWHM bandwidth of the beam, thereby including 95% of the bandwidth. Accordingly, we estimate the upper bound for the bandwidth effect at the first maximum to be twice that calculated at $20.010 \pm 0.001\,57$ keV. At these energies the applied linearized correction is less than around 0.03% (from Fig. 12), and so an upper bound of 0.06% is established. The error arising from the use of the linearized approximation is significantly less than this upper bound for the measurements made around the more weakly curved extrema in the XAFS region. The error arising from
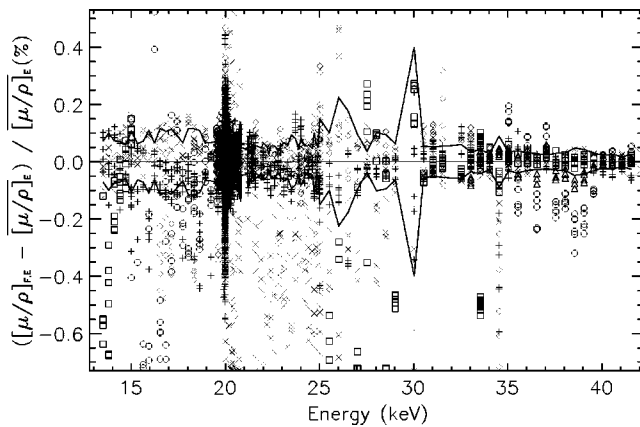
FIG. 13. The percentage discrepancies of individual measurements from the weighted mean after correction for the effect of the bandwidth. Only those measurements falling within a small range of the zero line are shown. The line indicates the σ_{sd} uncertainty in the weighted mean determined from Eq. (A3).

the use of the linearized approximation is generally well below the measurement uncertainty in the XAFS region.

Allowance for the bandwidth effect results in a reduction of the χ_r^2 from $\chi_r^2 = 3.94$ to 3.63. This reduction is quite significant considering that only a small fraction of the data are corrected by more than 0.03%.

2. Residual discrepancies and their treatment

The percentage discrepancies between the measurements after correction for the bandwidth effect are presented in Fig. 13. Here we show only the results within a small range of the zero line since the discrepancies are very similar to those presented in Fig. 5. Included on this plot is a line marking the one-standard-deviation uncertainty in the weighted mean, σ_{sd}, determined as the weighted uncertainty multiplied by the χ^2 of the population by use of

$$\sigma_{sd} = \sigma_{\overline{[\mu/\rho]}_{E_i}} \tag{A2}$$

$$= \left(\sum_{F_j} \frac{([\mu/\rho]_{E_i F_j} - \overline{[\mu/\rho]}_{E_i})^2}{\sigma^2_{[\mu/\rho]_{E_i F_j}}} \middle/ \sum_{F_j} \frac{1}{\sigma^2_{[\mu/\rho]_{E_i F_j}}} \right)^{1/2}, \tag{A3}$$

where the summation is over all measurements F_j at each energy, and $\overline{[\mu/\rho]}_{E_i}$ is the weighted mean of the measurements at each energy. This σ_{sd} properly quantifies our uncertainty in the weighted mean for measurements that are not necessarily consistent within their individual uncertainties.

The σ_{sd} uncertainty is typically below about 0.07%. At a number of energies between 25 and 30 keV the uncertainty associated with the measurement rises due to instabilities in the apparatus and adjustments of the settings made during the course of the experiment. The complex of discrepancies occurring near the absorption edge is still present in this plot and has resulted in a slight increase in the σ_{sd} uncertainty in that region.
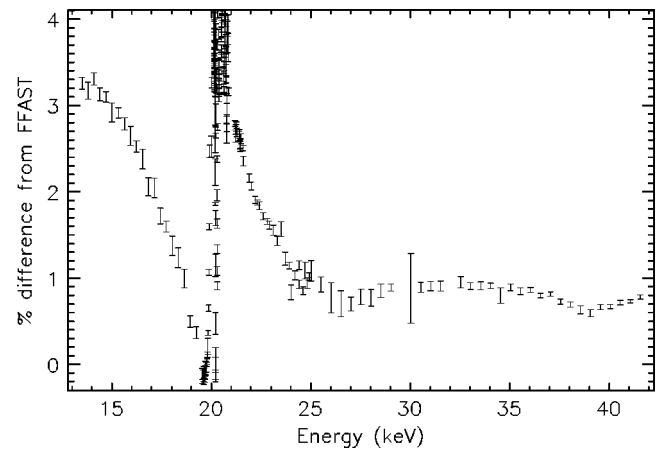
FIG. 14. Percentage difference between the measured mass attenuation coefficients and the FFAST tabulation. By comparing the measured values with a smooth and near-lying result we are able to examine closely the trend of the measured values. This plot demonstrates that the trend of the measured values is continuous to within their estimated uncertainties.

The minimization of the differences between measurements made at each energy does not alter the relationship between measurements made at different energies. In order to examine closely the smoothness of the measurements we calculate the percentage difference between the measured values and a near-lying and smooth function. In Fig. 14 we have used for this purpose the interpolated results of the FFAST calculation. The measured values fall on a continuous and smooth curve to within the determined uncertainty. The correspondence between the measurement variation and the uncertainties confirms the procedure used to estimate the uncertainties.

We have tested the measurement for further systematic errors. These tests have employed a number of approaches including (i) statistical analysis (t test) of differences between subsets of the measurement population; (ii) comparison of the predictions of the correction equation [for example, Eq. (A1)] against the observed discrepancies (Figs. 5 and 13); (iii) fitting the results to test for the presence of trial systematic errors; and (iv) interpretation of on-line diagnostic measurements. In the following subsections we will briefly describe these investigations and their findings.

a. Secondary photons

There is no significant difference between the results obtained with different aperture sizes. This is in agreement with modeling of scattering processes and aperture sizes. The apertures used probe one-tenth of the range of solid angles reported in [41]. We therefore predict the effect to be significantly smaller than that observed in [41], and estimate a maximum correction of 0.01–0.02 %, which is below the sensitivity of our measurements.

b. Beam harmonic content

Daisy wheels were used to make measurements using a large number of molybdenum and aluminum absorbers with

attenuations typically covering the range $0.05 \lesssim [\mu/\rho][\rho t] \lesssim 30$. These attenuations have been analyzed following Ref. [27], yielding a maximum effective beam harmonic content of less than about a 10^{-4} fraction of harmonic photons at all energies measured in this experiment.

The beam harmonic content was also tested by attempting to fit the mean beam harmonic fraction to the results of the attenuation measurements. Here we used a correction equation similar to that in [27], but refined to include the energy dependence of the ion-chamber efficiencies and the air absorption. This fitting determined an average harmonic component that was consistent with zero, with the sensitivity of the diagnostic at around 1 in 10^4 photons.

These diagnostics indicate that the detuning of the monochromator successfully suppressed the harmonic components and their effect on the result was insignificant.

c. The effect of roughness

The effect of roughness in the integrated column density [23,31] was checked by use of the fitting procedure. In this case the fitted parameters were the rms deviations of the integrated column density $\sigma_{[\rho t]}$ for each of the foils. The effect was found to be consistent with zero, confirming the absence of a systematic error due to sample roughness and voids within the sample volume.

d. Linearity of the detection system

In order for an attenuation measurement to be accurate, the detectors and counting chain must be linear over the range of the measured intensities. It is difficult to guarantee the linearity of the ion chambers and the detection chain to the level of precision indicated by Fig. 13, of order 0.07%, without performing explicit tests.

A number of effects can lead to nonlinearities in the detector and counting chain. It is beyond the scope of this article to discuss all physical mechanisms responsible for detector nonlinearity. Instead we consider the possibility of a nonlinear response in the current amplifiers and the counting chain used in this experiment.

One consequence of the energy dependence of the ion-chamber detection efficiencies is that we have had to manually adjust the electronic gain settings on the current amplifiers. When these gain settings were altered, usually by a factor of 2 or 5, any effect of nonlinearities in the current amplification and counter scaling might be observed as a discontinuity in the measured attenuations. However, such discontinuities are not present in the measured data presented in Fig. 14, and thus such effects are insignificant in this experiment.

Nonlinearities resulting from the molecular dynamics within the detector volume can be investigated by examining discrepancies between the results of measurements using very different incident beam intensities. In this experiment the incident x-ray intensity decayed to around half of its initial value over the course of 12 h, at which time electrons were injected into the synchrotron ring to return the beam intensity to its initial value.

We have used the pre- and postinjection period as an opportunity to test the effect of intensity variations on the measurements of the mass attenuation coefficient. We found *no* significant discontinuities in the results measured immediately before and after the beam injections and conclude that the response of the counting chain is linear to the level of the claimed uncertainties in the relevant high-count region.
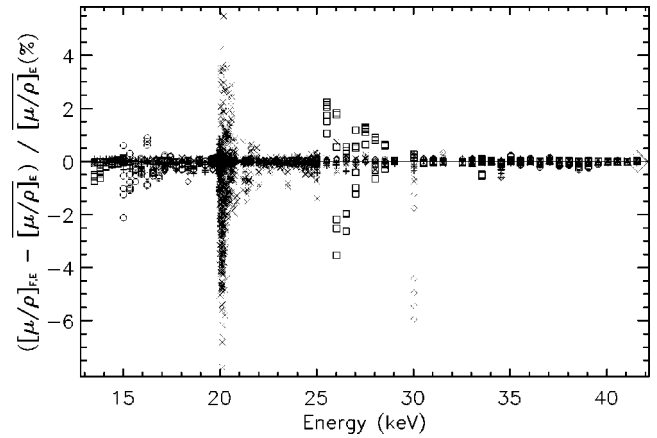
e. Residual discrepancies

A residual systematic deviation of the measurements made with the thickest foil is clearly present in Fig. 5. The low precision of the measurements contributing to the dominant signature, results in the low significance of this residual, as seen from Fig. 6. These residual deviations can be due to a residual harmonic component in the synchrotron beam, a poorly determined dark current, or sample roughness. The extremely low $\Delta\chi_r^2$ attached to this residual signature gives rise to a similar pattern of discrepancy for each source of error.

We have corrected the systematic deviations present in Fig. 5 by treating the residual deviations as if they were the result of an incorrectly determined dark current in the downstream ion chambers. This dark-current error is corrected according to

$$\left[\frac{\mu}{\rho}\right] \rightarrow \left[\frac{\mu}{\rho}\right]' = \left[\frac{\mu}{\rho}\right] + \frac{1}{[\rho t]}\frac{\Delta_{dc}}{I_{d,s}}, \qquad (A4)$$

where the fitted parameter Δ_{dc} describes the offset to the measured dark-current value in the downstream detectors. In this fitting a single value of Δ_{dc} is used for each period in which the ion-chamber electronics settings remained unaltered.

In Fig. 15 we present the percentage discrepancies of the measured mass attenuation coefficients after fitting for this signature. The agreement between the measurements across a wide range of energies is qualitatively improved, indicating that this correction is of the correct form and magnitude. The change to the weighted mean arising from this correction is

FIG. 15. The percentage discrepancies of measurements from the weighted mean, after correction for the effect of the residual discrepancy. The four large systematic divergences seen in Fig. 5 are now centered about the zero line. The reported uncertainty is the uncertainty of the weighted mean added in quadrature to one-quarter of the present correction.

less than the original uncertainty for all measurements except those between 25–30 keV. To account for the model uncertainty and the small remnant signature of the deviations we have added a further uncertainty to these measurements equal to one-quarter of the magnitude of the correction.

3. The rejection of corrupted measurements

In a highly automated large experimental run it is almost inevitable to end up with some procedural errors.

In response to a number of experimental variables such as the changing detector efficiencies and sample attenuations, and the energy dependence of the undulator spectrum, the apparatus and the experimental settings were adjusted and optimized a number of times during the five days in which measurements were made. The results have been examined closely to determine situations in which the measurements exhibited systematic deviations and low accuracy. Where such deviations are present in the data we have investigated the measurements to determine the cause of their inconsistency. Where possible we have isolated the affected data and discarded them from the measurement. In this section we will briefly detail inconsistencies observed in the data and their treatment.

The time taken for the beamline shutter to open and close resulted in the recording of a number of 0.1 s measurements before the shutter had completed its motion. The incomplete motion of the shutter, which was located upstream of the monitor counter and was evidenced by the monitor count, typically affected only the first two measurements in each series of ten. Around 2300 out of 78 000 measurements were affected by the incomplete shutter motion and were rejected from the data set.

Measurements recorded immediately after the daisy wheel was rotated to the position of the smallest aperture were affected by a small vibration in the daisy wheel, which led to some clipping of the x-ray beam. This resulted in a large variation in the measured downstream intensity which, unlike the shutter problem, was uncorrelated with the monitor count. The high correlation coefficient ($R \approx 0.99$) between the measurements recorded with the upstream and downstream ion chambers enabled us to easily identify and reject the affected measurements.

In the energy range between 20.17 and 20.9 keV measurements were made with a higher than appropriate counter am-

plification setting in the downstream ion chambers. The effect of this was to cause the amplifier output voltage on some occasions to exceed the scaler's input range, leading to what we shall refer to as "counter saturation." This counter saturation is akin to reaching the full-scale deflection of a measuring instrument, and does not necessarily imply a loss of linearity of nonsaturated measurements. As it turned out, the counters were just barely saturated and only some of the measurements were affected. Counter saturation in downstream ion chambers affected only the high-intensity measurements, i.e., the unattenuated normalized intensities I_b, made with the sample removed from the beam. The removal of the saturated measurements from the data set was again facilitated by the high correlation of the counts recorded in the upstream and downstream ion chambers. The rejection of some measurements from each series of ten results in a greater uncertainty for I_b; however, there is no significant decrease in the overall precision of the counter-saturated measurements as the precision of I_b turned out not to limit the experimental precision.

The measurements made at energies between 20.9 and 21.19 keV were also affected by counter saturation. However, here the measurements recorded in both of the downstream ion chambers were fully saturated and could not be recovered.

A significant proportion of the results in the region of the XAFS have been determined from measurements using only a single foil. As a result, these results do not necessarily share the same baseline as the results derived from the weighted mean of many measurements. Correction of the measurement discontinuities in the XAFS region is particularly appropriate for subsequent XAFS partial-wave analysis. We treated these single-foil measurements as being on a relative scale and placed them on an absolute scale by comparing them with neighboring weighted-mean values. These data have been rescaled by an amount that is less than the uncertainty in the measurements, so any analysis correctly propagating input uncertainties will be unaffected by this procedure.

Measurements recorded with a single foil whose attenuation was $[\mu/\rho][\rho t] \approx 8$ in the XAFS region have been omitted because the high attenuation of this foil resulted in a low precision of these values of about 1–3 %. This has resulted in the gaps in the measurement seen in Fig. 9.

[1] C. T. Chantler *et al.*, Phys. Rev. A **64**, 062506 (2001).

[2] C. Q. Tran, C. T. Chantler, Z. Barnea, D. Paterson, and D. J. Cookson, Phys. Rev. A **67**, 042716 (2003).

[3] M. S. Freedman and F. T. Porter, Phys. Rev. A **6**, 659 (1972).

[4] D. W. Lindle *et al.*, Phys. Rev. A **38**, 2371 (1988).

[5] P. Weightman, E. D. Roberts, and C. E. Johnson, J. Phys. C **8**, 550 (1975).

[6] M. O. Krause and J. H. Oliver, J. Phys. Chem. Ref. Data **8**, 329 (1979).

[7] Y. Joly, D. Cabaret, H. Renevier, and C. R. Natoli, Phys. Rev.

Lett. **82**, 2398 (1999).

[8] D. Sayers, E. Stern, and F. Lytle, Phys. Rev. Lett. **27**, 1204 (1971).

[9] Y. Joly, Phys. Rev. B **63**, 125120 (2001).

[10] C. T. Chantler, C. Q. Tran, D. Paterson, D. J. Cookson, and Z. Barnea, Phys. Lett. A **286**, 338 (2001).

[11] C. T. Chantler, J. Phys. Chem. Ref. Data **29**, 597 (2000).

[12] C. T. Chantler, J. Phys. Chem. Ref. Data **24**, 71 (1995).

[13] C. T. Chantler *et al.*, http://physics.nist.gov/ffast

[14] J. H. Hubbell, *Bibliography of Photon Total Cross Section (At-*

tenuation Coefficient) Measurements 10 eV to 13.5 GeV, 1907–1993, NISTIR 5437 (National Institute of Standards and Technology, Gaithersburg, MD, 1994).

[15] J. H. Hubbell, J. S. Coursey, J. Hwang, and D. S. Zucker, *Bibliography of Photon Total Cross Section (Attenuation Coefficient) Measurements* (version 2.3) (National Institute of Standards and Technology, Gaithersburg, MD, 2003), available at http://physics.nist.gov/photoncs

[16] M. J. Berger and J. H. Hubbell, *XCOM: Photon Cross Sections on a Personal Computer*, NBSIR 87–3597 (National Bureau of Standards, Gaithersburg, MD, 1987).

[17] M. J. Berger, J. H. Hubbell, S. M. Seltzer, J. S. Coursey, and D. S. Zucker, *XCOM: Photon Cross Section Database* (version 1.2) (National Institute of Standards and Technology, Gaithersburg, MD, 1999), available at http://physics.nist.gov/xcom

[18] D. C. Creagh and J. H. Hubbell, Acta Crystallogr., Sect. A: Found. Crystallogr. **43**, 102 (1987).

[19] D. C. Creagh and J. H. Hubbell, Acta Crystallogr., Sect. A: Found. Crystallogr. **46**, 402 (1990).

[20] http://www.espimetals.com/

[21] http://www.espimetals.com/metals/molybdenum.pdf

[22] J. Goulon, C. Goulon-Ginet, R. Cortes, and J. M. Dubois, J. Phys. (France) **43**, 539 (1982).

[23] C. Q. Tran, Z. Barnea, C. T. Chantler, and M. D. de Jonge, Rev. Sci. Instrum. **75**, 2943 (2004).

[24] https://beam.aps.anl.gov/pls/apsweb/ bd_display_pkg.display_beamline?i_beamline_id=1-ID

[25] J. H. Beaumont and M. Hart, J. Phys. E **7**, 823 (1974).

[26] U. Bonse, G. Materlik, and W. J. Schröder, J. Appl. Crystallogr. **9**, 223 (1976).

[27] C. Q. Tran *et al.*, X-Ray Spectrum. **32**, 69 (2003).

[28] C. T. Chantler, C. Q. Tran, D. Paterson, Z. Barnea, and D. J. Cookson, X-Ray Spectrum. **29**, 449 (2000).

[29] C. T. Chantler, C. Q. Tran, D. Paterson, D. J. Cookson, and Z. Barnea, X-Ray Spectrum. **29**, 459 (2000).

[30] B. Nordfors, Ark. Fys. **18**, 37 (1960).

[31] M. D. de Jonge, Z. Barnea, C. T. Chantler, and C. Q. Tran, Meas. Sci. Technol. **15**, 1811 (2004).

[32] B. D. Cullity, *Elements of X-Ray Diffraction* (Addison-Wesley, Reading, MA, 1956).

[33] R. D. Deslattes, E. M. Kessler, W. C. Sauder, and A. Henins, Ann. Phys. (N.Y.) **129**, 378 (1980).

[34] P. J. Mohr and B. N. Taylor, Rev. Mod. Phys. **72**, 351 (1998).

[35] S. Kraft, J. Stümpel, P. Becker, and U. Kuetgens, Rev. Sci. Instrum. **67**, 681 (1996).

[36] B. L. Henke, E. M. Gullikson, and J. C. Davis, At. Data Nucl. Data Tables **54**, 181 (1993).

[37] S. Brennan and P. L. Cowan, Rev. Sci. Instrum. **63**, 850 (1992).

[38] S. Brennan and P. L. Cowan, http:// www.bmsc.washington.edu/scatter/periodic-table.html.

[39] C. Q. Tran *et al.*, J. Phys. B **38**, 89 (2005).

[40] M. D. de Jonge, Z. Barnea, C. Q. Tran, and C. T. Chantler, Phys. Rev. A **69**, 022717 (2004).

[41] C. Q. Tran, M. D. de Jonge, Z. Barnea, and C. T. Chantler, J. Phys. B **37**, 3163 (2004).

[42] See EPAPS Document No. E-PLRAAN-71-012502 for a complete tabulation. The electronic tabulation includes further 425 measurements between 19.56 keV and 21.454 keV, made at energy intervals down to 0.5 eV. These further measurements include detailed x-ray-absorption near-edge structure (XANES) and EXAFS. A direct link to this document may be found in the online article's HTML reference section. The document may also be reached via the EPAPS homepage (http://www.aip.org/pubservs/epaps.html) or from ftp.aip.org in the directory/epaps/. See the EPAPS homepage for more information.